SPATIO-TEMPORAL ASSESSMENT OF URBAN HEAT ISLANDS AND FUTURE PREDICTION: A CASE STUDY OF KATHMANDU VALLEY USING OPTICAL REMOTE SENSING

Sandeep Gautam[1], Bibek Karki[1], Namrata Thapa[1], Subekshya Subedi[1]
[1]Department of Geomatics Engineering, Pashchimanchal Campus, IOE, Tribhuvan University, Pokhara, Nepal
pas077bge040@wrc.edu.np, pas077bge010@wrc.edu.np, pas077bge025@wrc.edu.np, pas077bge046@wrc.edu.np

KEY WORDS: Kathmandu Valley, LST, LULC, NDBI, NDVI, Urban Heat Island, Remote Sensing

ABSTRACT:

Kathmandu Valley has experienced among the most rapid and concentrated urban expansion in South Asia over the past two decades, with direct but incompletely characterised consequences for surface thermal conditions. This study assesses the spatio-temporal evolution of Urban Heat Islands (UHI) across the valley from 2008 to 2023 using multi-temporal Landsat imagery processed in Google Earth Engine (GEE), and projects land surface conditions to 2028. Land Use Land Cover (LULC) was mapped using a Random Forest (RF) classifier at five-year intervals; Land Surface Temperature (LST) was retrieved from thermal bands via an emissivity-corrected inversion. The Normalised Difference Vegetation Index (NDVI) and Normalised Difference Built-up Index (NDBI) were used to quantify vegetation cover and impervious surface intensity and their relationship with LST. A CA-Markov model was used for LULC projection to 2028, followed by RF Regression to forecast LST under projected land-cover conditions. Pearson's correlation analysis yielded $r = +0.751$ for LST–NDBI and $r = -0.759$ for LST–NDVI, both statistically significant. Built-up area expanded from 8,720 ha (9.32%) in 2008 to 18,525 ha (19.82%) by 2023, with mean LST peaking at 27.34°C in 2018. UHI intensity was highest in the central built-up core (class mean 1.00–1.19) and negative over forested hillsides (−0.91 to −0.83). By 2028 built-up cover is projected to reach 25.47% of the valley, with mean LST rising to approximately 26.88°C and the central thermal hotspot expanding further. These findings demonstrate that vegetation management and targeted greening in high-density wards can partially counteract UHI intensification, providing quantitative evidence to support climate-resilient land-use planning in the Kathmandu Valley.

1. INTRODUCTION

Global urban populations now exceed 4.2 billion and are projected to reach 6 billion by 2041 (Kuddus et al., 2020). As cities expand, natural land surfaces are progressively replaced by impervious materials such as concrete, brick, and asphalt, which alter the surface energy balance by reducing evapotranspiration and increasing sensible heat flux. This process gives rise to the Urban Heat Island (UHI) effect, a well-documented phenomenon in which urban cores are measurably warmer than surrounding rural zones (de Almeida et al., 2021; Kim and Brown, 2021).

In Nepal, where the national urban growth rate is approximately 3% per year, Kathmandu Valley represents the sharpest point of urban pressure. The valley accommodates close to a quarter of the country's urban population and has seen its built-up footprint expand more than fourfold between 1989 and 2016 (Ishtiaque et al., 2017). Prior research has established the broad outlines of this thermal problem, but with significant gaps. Sarif et al. (2020) documented LULC changes and their UHI consequences in the valley between 1988 and 2018 but did not produce quantitative LST–index correlations. Mishra et al. (2019) evaluated the NDVI–LST relationship from 2000 to 2018, confirming negative correlation but offering no future projections. Maharjan et al. (2021) placed Kathmandu among the most thermally intense cities in South Asia using multi-city comparisons, yet did not model future LULC or LST change. Most recently, Khatri et al. (2025) used GEE and CA-Markov to project UHI conditions to 2030, but did not couple those LULC projections to a machine-learning-based LST forecast. Collectively, these studies leave two gaps unaddressed: (i) the absence of a machine-learning-derived LST prediction conditioned on projected LULC, and (ii) a quantitative analysis of the NDVI–NDBI–LST relationships across multiple epochs within the valley.

The present study was designed to address both gaps. Using multi-temporal Landsat imagery processed in GEE alongside analysis conducted in QGIS and Python, a connected workflow spanning 2008 to 2028 was constructed. The specific objectives of this study are: (i) to produce LULC, NDVI, NDBI, and LST maps for four epochs - 2008, 2013, 2018, and 2023; (ii) to analyse spatio-temporal changes in each parameter and quantify their mutual relationships; (iii) to project LULC and LST conditions for 2028 using CA-Markov and RF Regression respectively; and (iv) to draw practical implications for UHI management in the valley. By integrating classification, spectral index analysis, spatial modelling, and machine-learning prediction into a unified framework, the study aims to provide a reproducible and evidence-based contribution to the growing body of remote sensing literature on Himalayan urban thermal environments.

2. STUDY AREA

Kathmandu Valley (85°11'–85°33'E; 27°24'–27°49'N) covers ~570 km² across three districts: Kathmandu, Lalitpur, and Bhaktapur. The bowl-shaped valley floor lies at ~1,400 m above sea level, enclosed by hills rising upto ~2,800 m that traps heat and pollutants, amplifying UHI intensity. The climate is subtropical highland (monsoon-influenced), with ~1,400 mm annual rainfall (June–September). Population surpasses 2.5 million, growing at ~6.5% per year , making it one of South Asia's fastest growing urban city, creating urgency for predictive UHI modeling (Timsina, 2020). The Bagmati River and tributaries surround the floor but face intense encroachment pressure.

Kathmandu Valley was selected as the study area for four reasons: (1) it holds nearly one-quarter of Nepal's urban population, making UHI effects particularly consequential for human health and energy demand; (2) its bowl-shaped topography (1400 m floor, surrounded by ~2800 m hills) traps heat and pollutants, amplifying UHI intensity; (3) urban growth rate (~6.5% annually) ranks among the fastest in South Asia, creating urgency for predictive UHI modeling; and (4) previous studies documented 7–9°C center-rural temperature differentials, establishing a baseline for comparison.

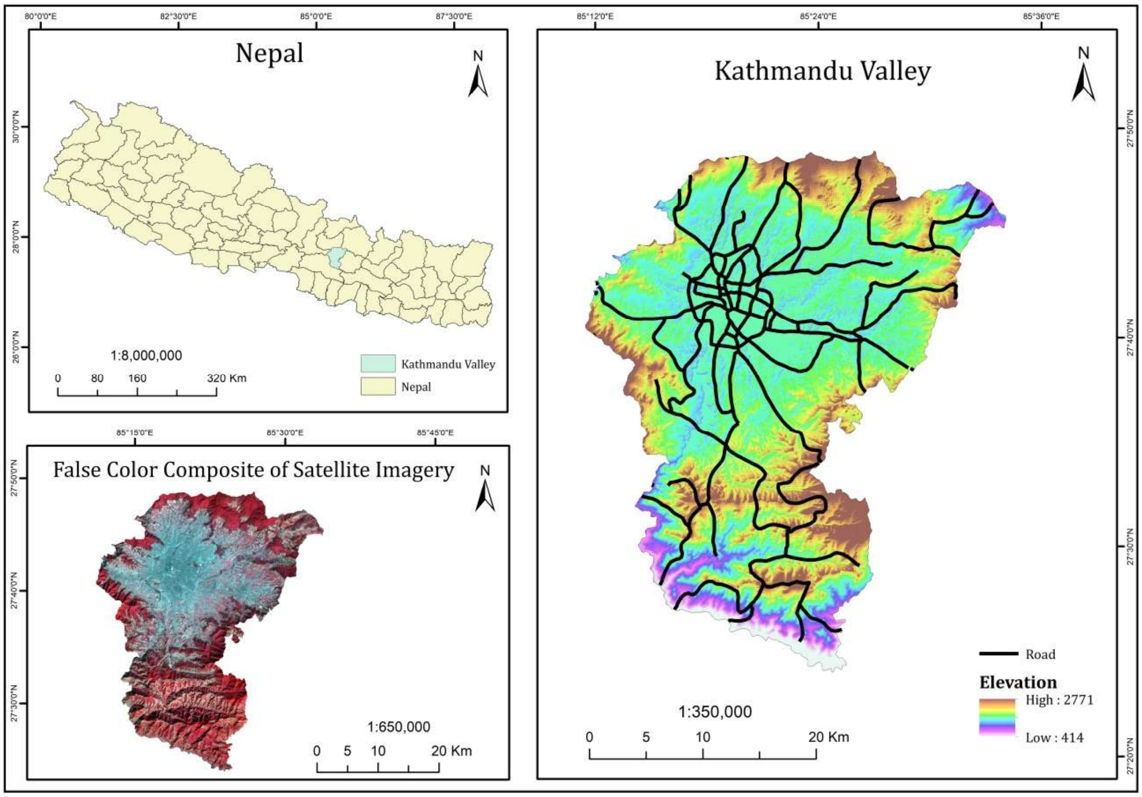

Figure 1. Kathmandu Valley study area: administrative boundary, elevation (SRTM), and road network

3. DATASETS AND METHODS

3.1 Data Sources

Landsat 8 OLI/TIRS (30/100 m) was used for 2013, 2018, and 2023 and Landsat 5 TM (30/120 m) for 2008, all sourced from the GEE catalog with minimal cloud cover. MODIS MOD11A1.061 (1 km daily LST) provided independent validation data. Ancillary data comprised the valley administrative boundary (Survey Department), road network (ICIMOD), and SRTM DEM (30 m).

Table 1. Datasets used in the study

Dataset	Source	Resolution	Epoch
Landsat 8 OLI/TIRS	GEE Catalog	30/100 m	2013, 2018, 2023
Landsat 5 TM	GEE Catalog	30/120 m	2008
MODIS MOD11A1.06	GEE Catalog	1 km	2013 (validation)
Valley Boundary	Survey Dept.	1:1,000,000	–
Road Network	ICIMOD	1:250,000	–
DEM (SRTM)	NASA	30 m	–

3.2 Workflow Overview

The end-to-end methodological workflow is illustrated in Figure 2. Spectral processing, classification, and index computation were carried out in GEE. LULC change analysis and CA-Markov simulation were conducted in QGIS using the MOLUSCE plugin. Pearson's correlation analysis, RF Regression modelling, and raster sampling were performed in Python (Jupyter Notebook) using Scikit-learn and Rasterio.

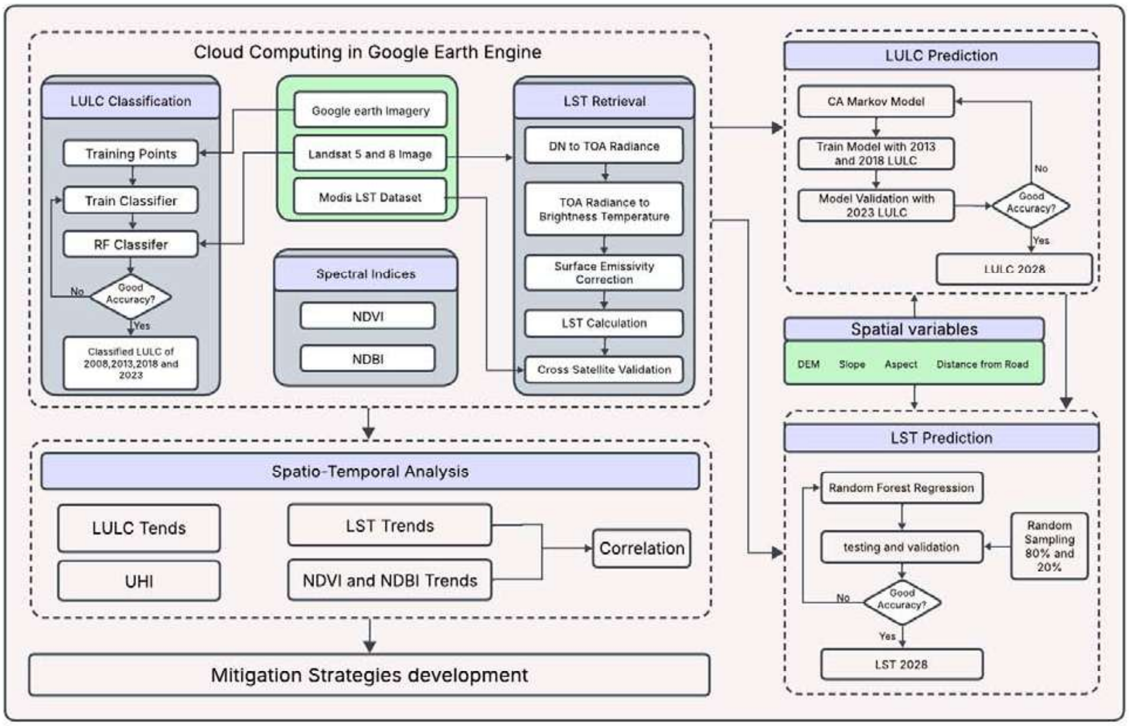

Figure 2. Methodological workflow from data acquisition to UHI prediction for 2028

3.3 LULC Classification

To minimise the influence of seasonal vegetation phenology and residual cloud cover, median annual composites were constructed for each study epoch within GEE. Reference points for five land-cover classes: Forest, Built-up, Water, Agriculture, and Barren were collected by visual interpretation of the Landsat composites alongside Google Earth Pro high-resolution imagery. Training samples per epoch were collected and divided 80:20 into training and validation subsets, ensuring spatial independence between the two sets. A Random Forest (RF) classifier with an ensemble of 100 decision trees was applied; final class assignment for each pixel was determined by majority vote across the trees (Tikuye et al., 2023). Map accuracy was assessed using overall accuracy (OA) and the Kappa coefficient (κ), computed as follows:

$$Overall\ Accuracy\ (\%) = \frac{Correctly\ Classified\ Pixels}{Total\ Reference\ Pixels} * 100 \quad (1)$$

$$\kappa = \frac{Samples * Corrected\ Samples - \sum(column\ total * row\ total)}{(Total\ Sample)^2 - \sum(column\ total * row\ total)} * 100 \quad (2)$$

3.4 LST Retrieval

LST was derived from the thermal band of each Landsat acquisition: Band 10 for Landsat 8 (central wavelength 10.8 µm) and Band 6 for Landsat 5 (central wavelength 11.5 µm) following a standard four-stage radiometric inversion procedure. First, digital numbers were converted to top-of-atmosphere (TOA) spectral radiance using the gain and offset coefficients provided in the image metadata. Second, brightness temperature was calculated from the TOA radiance using the Planck function. Third, land surface emissivity (ε) was estimated from the NDVI-derived fractional vegetation cover (Pv), following the approach of Sobrino et al. (2004), as expressed in Equations (3) and (4). Fourth, LST was retrieved by solving the radiative transfer equation, given in Equation (5):

$$\varepsilon = 0.004 \times Pv + 0.986 \quad (3)$$

$$Pv = \left(\frac{NDVI - NDVImin}{NDVImax - NDVImin}\right)^2 \quad (4)$$

$$LST = \frac{T}{1 + \left(\frac{\lambda \cdot T}{\rho}\right) \cdot ln(\varepsilon)} \quad (5)$$

where T is the at-satellite brightness temperature (K), λ is the band-centre wavelength (10.8 µm for Landsat 8; 11.5 µm for Landsat 5), and $\rho = hc/\sigma = 1.438 \times 10^{-2}$ m·K (h = Planck's constant, c = speed of light, σ = Boltzmann constant). The resulting LST raster was upsampled from 100 m to 30 m by bilinear resampling to maintain spatial consistency with the optical bands.

3.5 Spectral Indices

3.5.1 NDVI.

$$NDVI = \frac{NIR - RED}{NIR + RED} \quad (6)$$

The Normalised Difference Vegetation Index was originally proposed by Tucker (1979) as a measure of green vegetation density and photosynthetic activity. It was used in this study to quantify the temporal change in surface vegetation cover across the valley and to examine its inverse relationship with LST. For Landsat 8 the NIR and RED inputs corresponded to Bands 5 and 4; for Landsat 5, Bands 4 and 3 were used. NDVI values above 0.60 indicate dense, healthy canopy; 0.20–0.60 represents moderate or sparse vegetation; values between 0.0 and 0.20 are typical of bare soil or impervious surfaces; and negative values are diagnostic of open water.

3.5.2 NDBI.

$$\text{NDBI} = \frac{\text{SWIR} - \text{NIR}}{\text{SWIR} + \text{NIR}} \tag{7}$$

The Normalised Difference Built-up Index was introduced by Zha et al. (2003) to delineate impervious urban surfaces from satellite imagery. It was selected for this study because it serves as a direct spectral indicator of built-up intensity linked to the formation of Urban Heat Islands (UHI). For Landsat 8, SWIR and NIR corresponded to Bands 6 and 5; for Landsat 5, Bands 5 and 4 were used. Positive NDBI values indicate built-up or barren surfaces; negative values correspond to vegetated or water-covered areas.

3.6 UHI Intensity

Rather than relying on absolute LST thresholds which vary year to year with atmospheric conditions, UHI intensity was expressed as a standardised thermal anomaly relative to the valley-wide mean for each epoch:

$$\text{UHI} = \frac{Ts - Tm}{\text{SD}} \tag{8}$$

where Ts is the LST at a given pixel (°C), Tm is the valley-wide image mean LST, and SD is the image standard deviation of LST. Positive values identify pixels that are anomalously warm relative to the spatial mean; negative values indicate cooler surfaces. This standardised metric allows meaningful UHI comparison across epochs with differing absolute temperature levels.

3.7 Predictive Modelling

3.7.1 CA-Markov LULC Projection.

Future LULC for 2028 was projected using a Cellular Automaton–Markov (CA-Markov) model, implemented in the MOLUSCE plugin for QGIS, an approach demonstrated by Muhammad et al. (2022) for spatio-temporal LULC forecasting. The model comprises two coupled components. The Markov Chain component computes a transition probability matrix from two historical LULC maps, quantifying the likelihood of each land-cover class transitioning to every other class over a defined time interval. The Cellular Automaton component uses these probabilities alongside spatial contiguity rules and driver layers to simulate the geographic pattern of change. In this study, transition potentials were trained on the 2013 and 2018 LULC maps using an Artificial Neural Network (ANN) multilayer perceptron. Spatial driver variables incorporated into the transition potential model were: DEM, slope, aspect, and Euclidean distance from the road network. The calibrated model was subsequently run five years forward from the 2023 classification to generate the 2028 LULC projection. Model performance was assessed by comparing the simulated 2023 LULC against the independently produced 2023 classified map, using percentage correctness and the Kappa coefficient.

3.7.2 RF Regression for LST Forecasting.

LST for 2028 was forecasted using a Random Forest Regression model, following the framework applied by Waleed et al. (2023) for urban thermal field prediction. Training data consisted of all historical epoch observations (2008, 2013, 2018, 2023) for which both measured LST values and spatial predictor layers were available. Predictor variables were: LULC class (encoded as integer), DEM, slope, aspect, and Euclidean distance from the road network, all resampled to a common 30 m grid. The training and test subsets were divided 80:20 using a random split to ensure that test pixels were independent of training pixels. Model performance was evaluated on the held-out test set using four metrics: the coefficient of determination (R^2) which explains the proportion of variance in LST accounted for by the model (0 to 1 scale), Root Mean Square Error (RMSE, °C) which measures the average deviation (in °C) between predicted and actual LST values with lower RMSE indicating better model precision, Mean Square Error (MSE, °C²)quantifies the squared errors, penalizing larger deviations more heavily than smaller ones, and Mean Absolute Error (MAE, °C) which represents the absolute average error. Once validated, the model was applied to the projected 2028 LULC raster alongside the static driver layers (DEM, slope, aspect, road distance) to generate a spatially continuous LST forecast surface for 2028. UHI intensities for 2028 were subsequently derived from that surface using Equation (8).

3.8 Validation

Two independent validation strategies were employed to assess the reliability of the LST retrieval. First, cross-sensor validation was conducted for the 2013 epoch by comparing the Landsat 8-derived LST surface against the contemporaneous MODIS MOD11A1.061 daily LST product. The Landsat LST raster was spatially aggregated to match the 1 km MODIS grid using a mean resampling kernel, and Pearson's correlation coefficient was computed between the two surfaces across all valley pixels for which valid MODIS retrievals existed. This provided an objective, sensor-independent check on the thermal inversion procedure. Second, spatial validation was performed by extracting mean LST values over two purposively selected study sites with contrasting urban density: Baneshwor, a dense commercial ward in central Kathmandu and Dholahity, a comparatively low-density residential area on the southwestern valley margin..

4. RESULTS AND DISCUSSIONS

4.1 LULC Change Analysis

Built-up area grew from 8,720 ha (9.32%) in 2008 to 18,525 ha (19.82%) in 2023 (net +9,805 ha).With this rate (around 654 ha/year) surpassing earlier estimates for 1989–2016 (Ishtiaque et al., 2017), it suggests that urbanization is picking up speed. Agriculture declined from 40,283 ha to 33,342 ha. Forest cover showed a modest net gain of ~3,310 ha on hillsides (Table 2, Figure 2). All four classified maps exceeded 80% OA and $\kappa >$ 0.75, confirming RF classification reliability.The built-up estimate for 2023 (19.82%) matches the findings of (Sarif et al., 2020; 18.9% for 2018) and (Khatri et al., 2025; 20.1% for 2023).

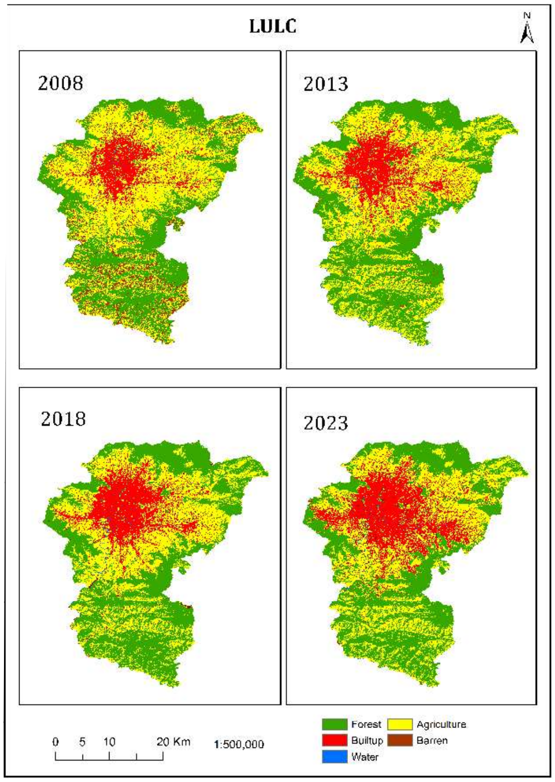

(a)

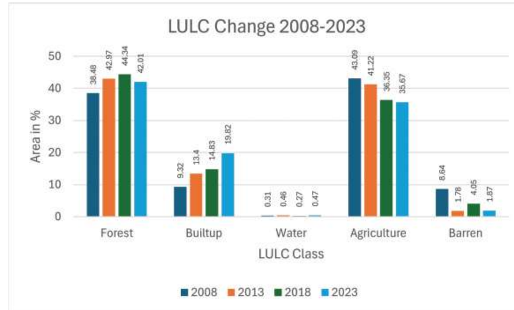

(b)

Figure 3. a) LULC classification maps for 2008, 2013, 2018, and 2023. b) Area change bar chart by class across epochs.

Table 2. LULC classification accuracy and built-up area summary

Year	OA	κ	Built-up (ha)
2008	0.84	0.78	8,720
2013	0.85	0.80	12,529
2018	0.92	0.90	13,859
2023	0.86	0.80	18,525

The transition probability matrix (Table 3) provides additional granularity on the sources of built-up expansion. Approximately 24% of all agricultural pixels present in 2008 had been converted to Built-up by 2023.The pattern indicates that urban expansion mainly takes place on agricultural land in the valley floor, rather than through deforestation on hillsides. This finding has policy implications: efforts to mitigate UHI should prioritize the preservation of remaining agricultural buffer zones over reforestation. Around 34% of water-body pixels experienced encroachment over the same interval, reflecting ongoing pressure on the Bagmati floodplain and its tributaries. By contrast, only 1.7% of Forest pixels transitioned to Built-up, indicating hill area conservation.

Table 3. Transition probability matrix 2008–2023

From \ To	Forest	Built-up	Water	Agri.	Barren
Forest	0.905	0.017	0.003	0.074	0.001
Built-up	0.010	0.841	0.013	0.112	0.025
Water	0.170	0.339	0.342	0.130	0.019
Agriculture	0.151	0.240	0.003	0.576	0.030
Barren	0.064	0.104	0.000	0.801	0.031

4.2 NDBI and NDVI Temporal Trends

Valley-wide mean NDBI shifted from −0.09 in 2008 to −0.19 in 2013 before recovering to −0.12 in 2018 and stabilising near −0.13 in 2023. The 2013 trough coinciding with relatively limited impervious surface growth in that interval is consistent with a period of slightly slower built-up densification and higher vegetation cover. At the class level, Built-up pixels consistently returned the highest NDBI values (near zero) across all epochs, while Forest pixels remained substantially negative (approximately−0.32), confirming the index's discriminative capacity for impervious surfaces.

Mean NDVI exhibited a complementary temporal pattern, peaking at 0.63 in 2013, the highest value across the entire study period before declining to 0.53 in 2018 and recovering marginally to 0.54 in 2023. The Built-up class recorded the lowest NDVI of any class in all four epochs (0.25–0.35), consistent with the sparse and fragmented nature of urban greenery. Forest class NDVI ranged between 0.62 and 0.80, confirming the integrity of hillside vegetation across the study period.The NDVI trend in central urban areas is declining, which indicates a gradual loss of vegetation. This suggests that urban growth is intruding on green spaces and diminishing the natural cooling effect of the valley. The growing NDBI trend, especially the growth of red zones in NDBI maps from 2008 to 2023, indicates a swift and ongoing densification of built-up areas, implying that urban sprawl is increasingly converting pervious surfaces into impervious ones.

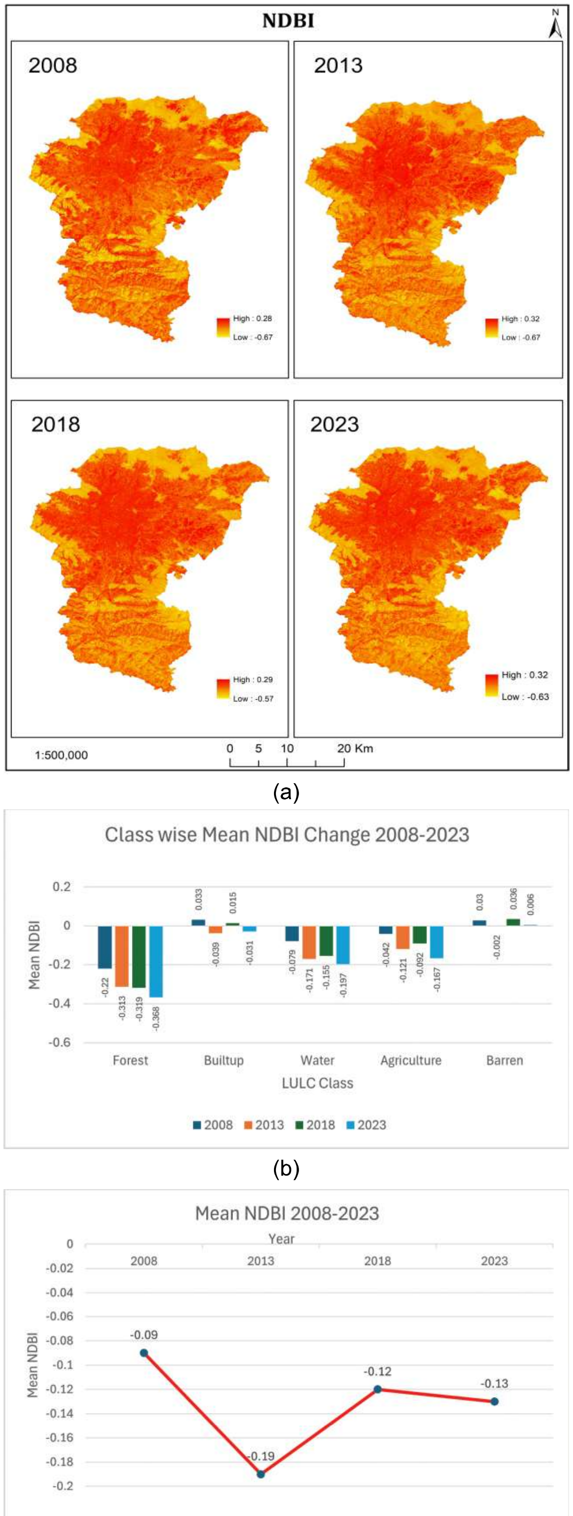

Figure 4. a) Temporal NDBI maps (2008–2023). b) Mean NDBI trend. c) Class-wise mean NDBI.

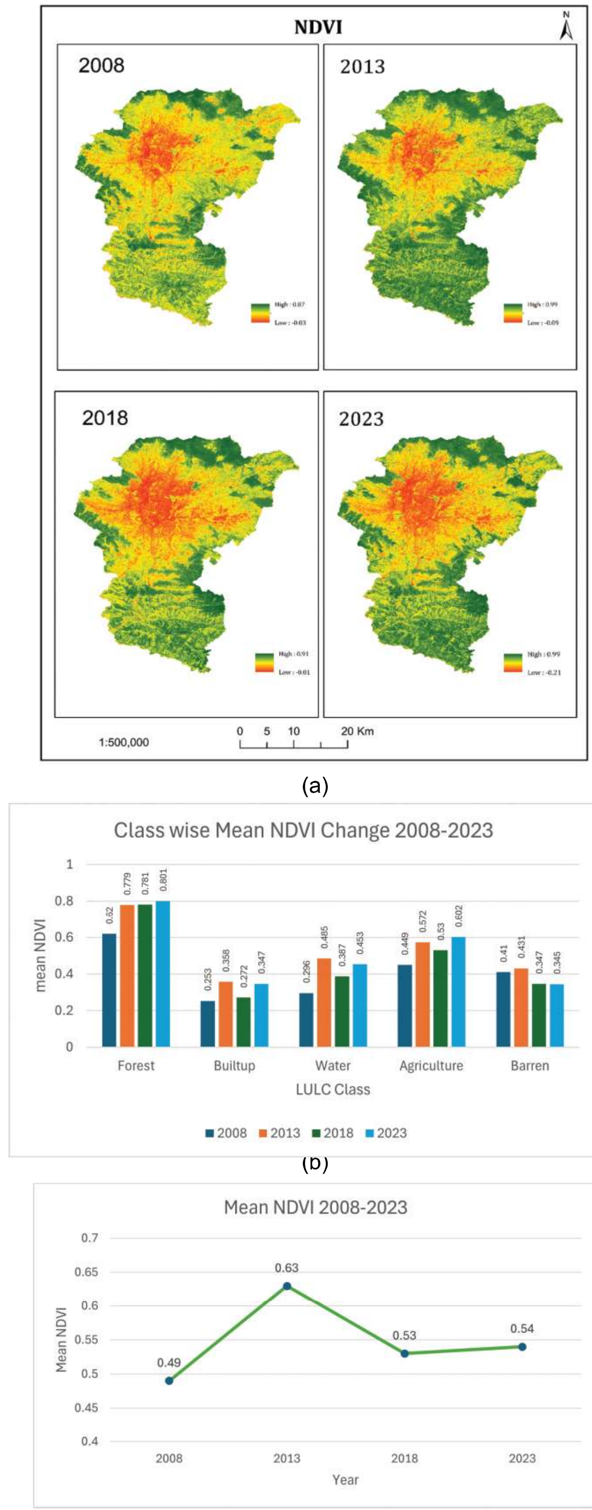

Figure 5. a) Temporal NDVI maps (2008–2023). b) Mean NDVI trend. c) Class-wise mean NDVI.

4.3 Land Surface Temperature

Mean valley-wide LST peaked in 2018 at 27.34°C and declined to 26.77°C by 2023, while pixel-level extremes revealed a 32.88°C range between dense built-up surfaces (42.87°C) and forested ridges (9.99°C), confirming that land cover type drives thermal contrast. The 2013 anomaly where mean LST fell by 1.23°C despite a 3,800 ha increase in built-up area is explained by the concurrent NDVI peak (0.63), providing direct empirical evidence that vegetation enhancement can offset urbanization-induced warming. Class-mean LST was consistently highest for Built-up (30.2–31.9°C) and lowest for Forest (22.3–24.3°C), with a persistent 7–9°C differential across all epochs, implying that any conversion of vegetated land to impervious surfaces will raise local LST by this magnitude. These findings align with Mishra et al. (2019), Sarif et al. (2020), and Khatri et al. (2025), and carry a clear policy implication: preserving forest cover and strategically expanding urban green spaces can meaningfully attenuate UHI even during active urban expansion.

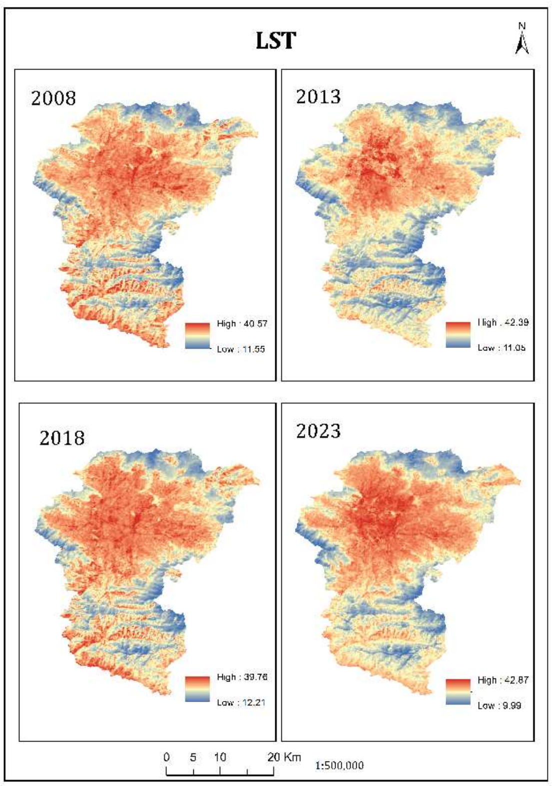

(a)

4.4 UHI Intensity

Built-up areas consistently exhibited the highest class-mean UHI intensity (1.00–1.19) while forested hillsides showed negative values (−0.91 to −0.83), confirming that the centralurban core functions as a persistent thermal hotspot and vegetated peripheries as cooling zones, consistent with Maharjan et al. (2021) and Sarif et al. (2020). The spatial gradient from dense inner-city districts like Baneshwor and Thamel outward to the peri-urban fringe implies that UHI intensity scales continuously with built-up density, suggesting that strategic greening of rapidly urbanizing fringe areasidentified by Ishtiaque et al. (2017) as agricultural zones undergoing conversioncould prevent them from becoming future hotspots. The maximum pixel UHI intensity peaked at 4.06 in 2013 despite that year having the lowest mean absolute LST, reflecting widened thermal contrast driven by the exceptionally high NDVI (0.63) which cooled vegetated surfaces sufficiently to amplify the relative warmth of the built-up core in the standardized metric. This finding carries a key policy implication: standardised UHI is a more sensitive indicator of thermal inequity than absolute LST alone, and policymakers should monitor both metrics simultaneouslyas recommended by Khatri et al. (2025)to avoid misinterpretation of greening intervention outcomes.

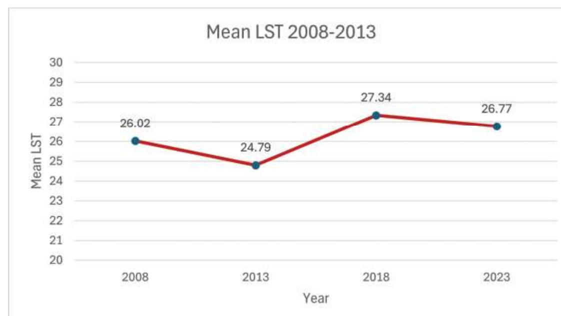

(b)

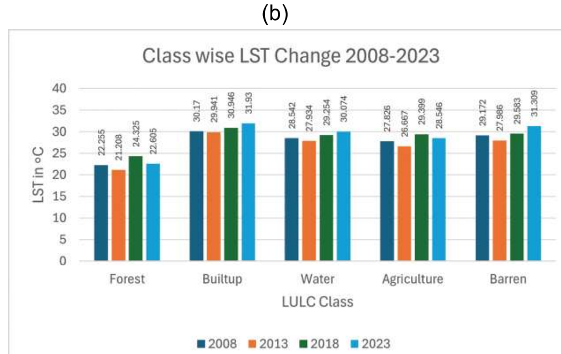

(c)

Figure 6. a) LST maps (2008–2023). b) Mean LST trend. c) Class-wise mean LST

4.5 Correlation Analysis

Pearson's correlation coefficients were computed from pixel-level co-registered composite rasters spanning all four study epochs. The investigation uncovers a robust positive correlation (r = 0.751) between land surface temperature (LST) and normalized difference built-up index (NDBI), signifying that built-up density is the primary thermal driver. In contrast, the negative correlation (r = -0.759) with the normalized difference vegetation index (NDVI) indicates that vegetation is the main cooling mechanism. These results correspond with comparable research conducted in Bangladesh and China, underscoring the near-symmetry of these relationships. Scatter plots (Figure 8) show linear relationships with no strong evidence of non-linearity that would compromise the Pearson's metric. The magnitude and symmetry of these two coefficients one positive, one negative, both of similar absolute value underscore the compensatory thermal role of vegetation relative to built-up cover

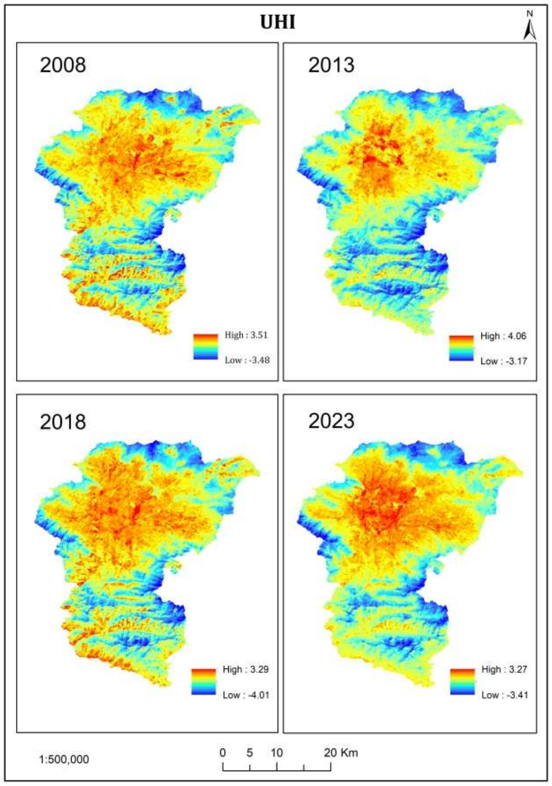

(a)

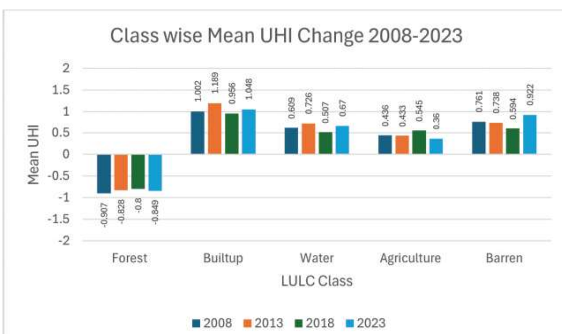

(b)

7. a) UHIintensity maps (2008–2023). b) Class-wise mean UHI values

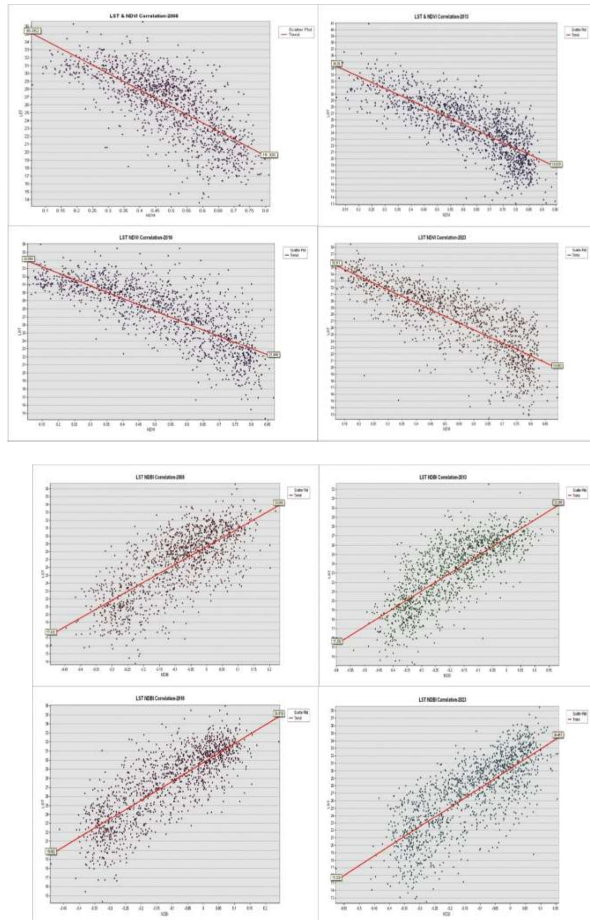

Figure 8. Pixel-level scatter plots: LST vs NDVI (top) and LST vs NDBI (bottom), all four epochs

4.6 Validation

Cross-sensor validation for 2013 was performed by aggregating the Landsat 8-derived LST raster to the 1 km MODIS grid using a mean resampling kernel, then computing Pearson's r between the two surfaces across all valid pixels within the valley boundary. The result was r = 0.95 (Figure 9), indicating strong agreement between the Landsat thermal inversion and the independent MODIS LST product. This provides objective evidence that the emissivity-corrected retrieval procedure is reliable for this study area and sensor configuration.

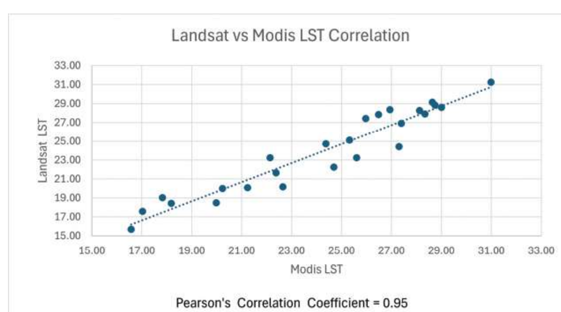

Figure 9. Cross Satellite Validation

Spatial validation using the two contrasting study sites returned mean LST values of 34.57°C at Baneshwor (high-density commercial) and 31.90°C at Dholahity (low-density residential), a differential of 2.67°C. Visual examination of contemporaneous Google Earth Pro imagery confirmed that Baneshwor is characterised by dense, contiguous impervious cover with minimal vegetation, while Dholahity retains a higher proportion of gardens, open land, and tree cover. The direction and magnitude of the temperature differential are therefore physically consistent with the NDBI–LST and NDVI–LST correlations established in Section 4.5, and support the interpretation that the LST maps accurately capture the spatial thermal gradient attributable to varying urbanisation intensity (Figure 10).

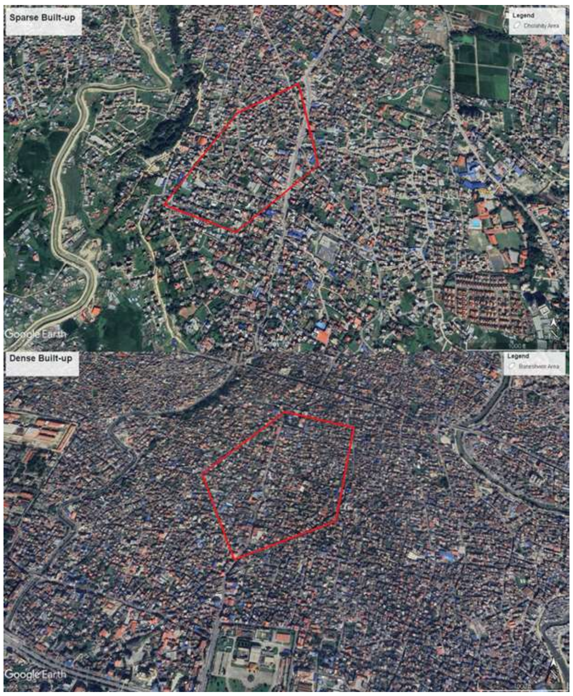

(a)

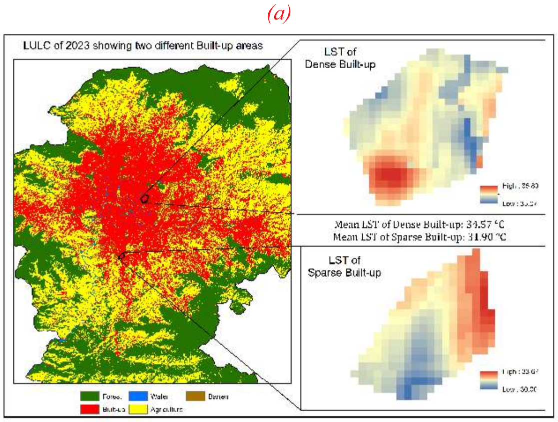

(b)

Figure 10. a) Google Earth Images of Baneshwor and Dholahity Area (2023). b)Validation Map

4.7 LULC and LST Prediction for 2028

4.7.1 LULC Projection.

The validation metrics of the CA-Markov model (overall correctness = 81.79%, κ = 0.714, κ-location = 0.82) surpass those reported by Muhammad et al. (2022) for Linyi, China (κ ≈ 0.68), indicating a reliable reproduction of spatial land-cover patterns. The 2028 projection indicates that the built-up area will reach 25.47% of the valley (+5.65 percentage points from 2023), mainly derived from Agriculture (−2.26 pp) and Forest (−1.53 pp)this aligns with Ishtiaque et al. (2017), who noted a fourfold increase in built-up area between 1989 and 2016. The anticipated reduction of water bodies to 0.23% mirrors the ongoing encroachment of rivers (34% converted to built-up areas by 2023), suggesting that without intervention, the valley's remaining surface waters are at risk of near-total loss, affecting local climate regulation as highlighted by Sarif et al. (2020).

Table 4. Projected LULC area changes from 2023 to 2028

Class	2023 (%)	2028 (%)	Change (%)
Forest	42.01	40.48	−1.53
Built-up	19.82	25.47	+5.65
Water	0.47	0.23	−0.24
Agriculture	35.67	33.41	−2.26
Barren	1.87	0.41	−1.46

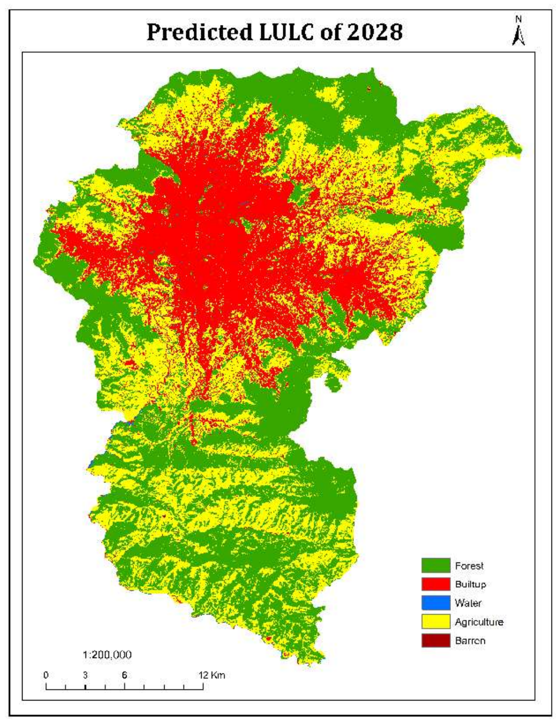

Figure 11. Predicted LULC map for 2028

4.7.2 LST and UHI Prediction.

The RF Regression model showed good performance ($R^2 = 0.817$, RMSE = 1.87°C), similar to Waleed et al. (2023), and predicts a mean LST of 26.88°C in 2028, with a maximum of 39.08°C in densely built-up regions. This extends the warming trend noted from 2008 to 2023 and corresponds with the projections of Khatri et al. (2025), who anticipated an intensification of UHI in the Kathmandu Valley by 2030. The UHI map generated indicates that the central hotspot is expanding toward the northwestern and eastern edges of the valley, suggesting that anticipated built-up growth will spread thermal inequity beyond the traditional urban core, in line with the findings of Sarif et al. (2020), who recorded outward UHI expansion due to peri-urban development.

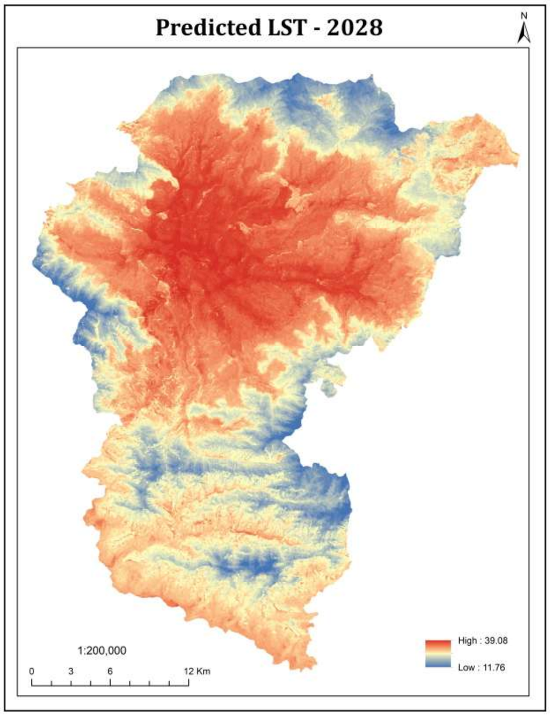

Figure 12. Predicted LST map for 2028

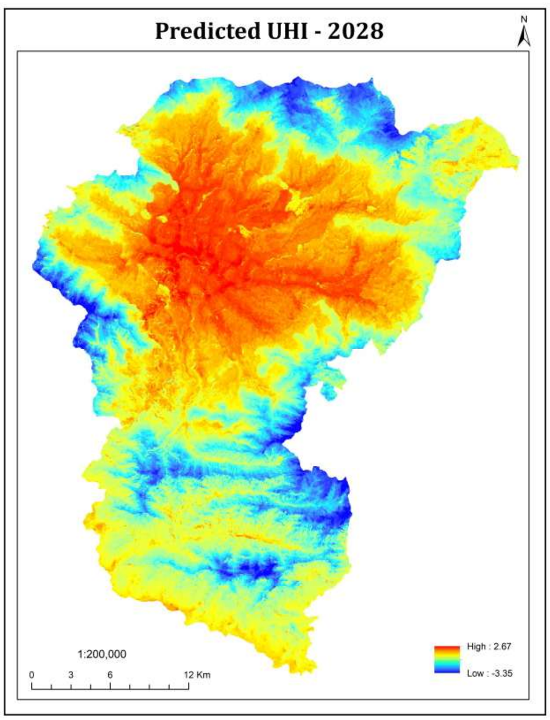

Figure 13. Predicted UHI intensity map for 2028

6. CONCLUSIONS

This study has produced a comprehensive spatio-temporal account of UHI dynamics in Kathmandu Valley spanning fifteen years (2008–2023), integrated with data-driven projections to 2028.Built-up land expanded by approximately 9,805 ha over the study period predominantly from agricultural land and water bodies while Forest cover recorded a modest net gain on the encircling hillsides. Mean LST ranged from 24.79°C (2013) to 27.34°C (2018), with the built-up class consistently recording class-mean values between 30.2 and 31.9°C across all epochs. LST was strongly and consistently correlated with both NDBI ($r = +0.751$) and NDVI ($r = -0.759$), confirming that impervious surfaces drive surface warming while vegetation suppresses it.

The 2013 epoch provides the study's most important practical insight: the anomalously high NDVI (0.63) in that year was sufficient to depress mean LST by 1.23°C despite concurrent built-up growth of ~3,800 ha. This is not merely a statistical artefact; it demonstrates that the thermal balance of the valley is genuinely sensitive to vegetation cover and that deliberate greening programmes can produce measurable thermal relief even within an actively urbanising context.

The 2028 projections built-up cover reaching 25.47%, mean LST of 26.88°C, maximum pixel LST of 39.08°C represent a plausible baseline scenario in the absence of policy intervention. The RF Regression model ($R^2 = 0.817$, RMSE = 1.87°C) provides a statistically defensible basis for this forecast, and the CA-Markov hindcast (correctness 81.79%, $\kappa = 0.714$) validates the LULC projection on which it rests. Together, these results establish a quantitative, reproducible evidence base for climate-resilient land-use planning in Kathmandu Valley. The integrated workflow - GEE-based spectral processing, RF LULC classification, CA-Markov simulation, and RF Regression forecasting is transferable to comparable mid-sized Himalayan and South Asian cities where Landsat coverage is available, offering a low-cost analytical pathway for cities with limited monitoring infrastructure.

ACKNOWLEDGEMENTS

The authors express sincere gratitude to Asst. Prof. Netra Bahadur Katuwal for his sustained guidance and constructive supervision throughout this research. They also thank the Department of Geomatics Engineering, Pashchimanchal Campus, Institute of Engineering, Tribhuvan University, for providing the institutional platform, laboratory resources, and software environment in which this work was conducted.

REFERENCES

Bhandari, S. and Zhang, C., 2022. Urban Green Space Prioritization to Mitigate Air Pollution and the Urban Heat Island Effect in Kathmandu Metropolitan City, Nepal. Land, 11(11), 2074. https://doi.org/10.3390/LAND11112074

Cetin, M., OzenenKavlak, M., SenyelKurkcuoglu, M.A., Bilge Ozturk, G., Cabuk, S.N. and Cabuk, A., 2024. Determination of land surface temperature and urban heat island effects with remote sensing capabilities: the case of Kayseri, Türkiye. Natural Hazards, 120(6), pp. 5509–5536. https://doi.org/10.1007/s11069-024-06431-5

de Almeida, C.R., Teodoro, A.C. and Gonçalves, A., 2021. Study of the urban heat island (UHI) using remote sensing data/techniques: A systematic review. Environments, 8(10), pp. 1–39. https://doi.org/10.3390/environments8100105

Ishtiaque, A., Shrestha, M. and Chhetri, N., 2017. Rapid Urban Growth in the Kathmandu Valley, Nepal: Monitoring Land Use Land Cover Dynamics of a Himalayan City with Landsat Imageries. Environments, 4(4), p. 72. https://doi.org/10.3390/ENVIRONMENTS4040072

Khatri, B., Kharel, B., Dhakal, P., Acharya, S. and Thapa, U., 2025. Spatio-temporal dynamics of urban heat island using Google Earth Engine: Assessment and prediction — A case study of Kathmandu Valley, Nepal. Climate Services, 38, p. 100560. https://doi.org/10.1016/J.CLISER.2025.100560

Kim, S.W. and Brown, R.D., 2021. Urban heat island (UHI) intensity and magnitude estimations: A systematic literature review. Science of the Total Environment, 779, p. 146389. https://doi.org/10.1016/j.scitotenv.2021.146389

Kuddus, M.A., Tynan, E. and McBryde, E., 2020. Urbanization: A problem for the rich and the poor? Public Health Reviews, 41(1), pp. 1–4. https://doi.org/10.1186/s40985-019-0116-0

Maharjan, M., Aryal, A., Man Shakya, B., Talchabhadel, R., Thapa, B.R. and Kumar, S., 2021. Evaluation of Urban Heat Island (UHI) Using Satellite Images in Densely Populated Cities of South Asia. Earth, 2(1), pp. 86–110. https://doi.org/10.3390/earth2010006

Mishra, B., Sandifer, J. and Gyawali, B.R., 2019. Urban Heat Island in Kathmandu, Nepal: Evaluating Relationship between NDVI and LST from 2000 to 2018. International Journal of Environment, 8(1), pp. 17–29. https://doi.org/10.3126/ije.v8i1.22546

Muhammad, R., Zhang, W., Abbas, Z., Guo, F. and Gwiazdzinski, L., 2022. Spatiotemporal Change Analysis and Prediction of Future Land Use and Land Cover Changes Using QGIS MOLUSCE Plugin and Remote Sensing Data. Land, 11(3), p. 419. https://doi.org/10.3390/LAND11030419

Rahman, M.N., Rony, M.R.H., Jannat, F.A., Pal, S.C., Islam, M.S., Alam, E. and Islam, A.R.M.T., 2022. Impact of Urbanization on Urban Heat Island Intensity in Major Districts of Bangladesh. Climate, 10(1). https://doi.org/10.3390/cli10010003

Sarif, M.O., Rimal, B. and Stork, N.E., 2020. Assessment of changes in land use/land cover and land surface temperatures in the Kathmandu Valley (1988–2018). ISPRS International Journal of Geo-Information, 9(12). https://doi.org/10.3390/ijgi9120726

Sobrino, J.A., Jiménez-Muñoz, J.C. and Paolini, L., 2004. Land surface temperature retrieval from LANDSAT TM 5. Remote Sensing of Environment, 90(4), pp. 434–440. https://doi.org/10.1016/j.rse.2004.02.003

Tikuye, B.G., Rusnak, M., Manjunatha, B.R. and Jose, J., 2023. Land Use and Land Cover Change Detection Using the Random Forest Approach: The Case of the Upper Blue Nile River Basin, Ethiopia. Global Challenges, 7(10), p. 2300155. https://doi.org/10.1002/GCH2.202300155

Timsina, N.P., 2020. Trend of urban growth in Nepal with a focus in Kathmandu Valley: A review of processes and drivers of change. Tomorrow's Cities Working Paper 001. www.tomorrowscities.org

Tucker, C.J., 1979. Red and photographic infrared linear combinations for monitoring vegetation. Remote Sensing of Environment, 8(2), pp. 127–150. https://doi.org/10.1016/0034-4257(79)90013-0

Waleed, M., Sajjad, M., Acheampong, A.O. and Alam, M.T., 2023. Towards Sustainable and Livable Cities: Leveraging Remote Sensing, Machine Learning, and Geo-Information Modelling to Predict Thermal Field Variance in Response to Urban Growth. Sustainability, 15(2). https://doi.org/10.3390/su15021416

Zha, Y., Gao, J. and Ni, S., 2003. Use of normalized difference built-up index in automatically mapping urban areas from TM imagery. International Journal of Remote Sensing, 24(3), pp. 583–594. https://doi.org/10.1080/01431160304987

AUTHOR INFORMATION

Name	:	**Sandeep Gautam**
Academic Qualification	:	BE in Geomatics Engineering
Organization	:	Geo3D Modelling
Current Designation	:	Geomatics Engineer
Work Experience	:	1 year
Published Article	:	2